Experiments in Fluids (2025) 66:172
https://doi.org/10.1007/s00348-025-04090-1

RESEARCH ARTICLE

Defocusing PTV flow measurements above a DBD plasma actuator array for oscillatory forcing

Saskia Pasch[1] · Heinrich L. Lange[1] · Robin Leister[1] · Jochen Kriegseis[1]

Received: 6 May 2025 / Revised: 9 July 2025 / Accepted: 20 July 2025
© The Author(s) 2025

Abstract

Lagrangian defocusing particle tracking velocimetry (defocusing PTV, DPTV) measurements are performed in a thin volume above a plasma actuator array that is applied to mimic the effect of wall oscillations by inducing alternating, wall-parallel forcing in opposite directions into the air above the actuator surface for flow control purposes. The aim of the experiments is to capture the plasma-induced flow topology in otherwise quiescent air throughout the oscillation cycle within the measurement volume of 14 mm × 1 mm × 14 mm, immediately adjacent to the wall-mounted actuator. For this purpose, particle image velocimetry equipment for time-resolved measurements with one camera is used in a DPTV setup, where the out-of-plane particle coordinate is obtained through the diameter of a defocused particle image. Three-dimensional, three-component velocity and acceleration data is extracted by introducing a continuous particle tracking approach and an extended ex situ calibration procedure based on the detection of solid particles directly applied to a wall boundary, for which no prior knowledge of the flow topology or velocity data in the direct vicinity of the wall is required. A novel method for estimating measurement uncertainty in this context is introduced, and the influencing factors are discussed from an application perspective. Through the analysis of Lagrangian particle tracks, both individual flow events and statistical effects within the oscillation cycle can be evaluated. The extraction of phase-resolved flow fields with adaptable spatial resolution shows the forcing effect to be regular across different discharge zones on the plasma actuator array, indicating well-balanced voltage settings and precise manufacturing. Furthermore, the relation between the forcing-induced velocity and acceleration fields is quantitatively assessed, revealing the spatio-temporal transmission characteristics of the applied forcing. In summary, the obtained results demonstrate the applicability of DPTV measurement technique for the flow characterization above a plasma actuator array using the presented modifications.

1 Introduction

Flow control strategies for turbulent skin friction drag reduction have gained considerable interest due to their power saving potentials. Streamwise-traveling waves of spanwise wall velocity have been shown to reduce surface drag in turbulent flows (Quadrio 2011; Marusic et al. 2021). As a potentially simpler implementation of such strategies, arrays of dielectric barrier discharge (DBD) plasma actuators (PA) have been introduced to mimic the effect of physical wall movement without previously required moving parts following the approach of convective (Benard et al. 2024), temporal (Wilkinson 2003; Jukes et al. 2006; Hehner et al. 2019, 2020) or combined spatio-temporal (Serpieri et al. 2023) wall oscillations.

DBD plasma discharges occur when an alternating voltage beyond the breakdown voltage induces a strong electric field across two electrodes, separated by a dielectric material (Kogelschatz 2003). Upon discharge, ionized particles are accelerated by the electric field, which effectively initiates an additional body force in the surrounding air. As a result, a predominantly horizontal momentum input develops above the lower, encapsulated electrode, thus emphasizing the suitability of DBD PAs for flow control applications. An overview of diagnostics application of PAs is provided in topical reviews on the topic, e.g., by Benard and Moreau (2014), Kotsonis (2015) and Kriegseis et al. (2016).

Figure 1 illustrates the multi-electrode PA array and beat-frequency operation mode used in this study, developed for temporally oscillating forcing by Hehner et al. (2020). The

✉ Jochen Kriegseis
jochen.kriegseis@kit.edu

[1] Institute of Fluids Mechanics (ISTM), Karlsruhe Institute of Technology (KIT), Kaiserstraße 10, 76131 Karlsruhe, Germany

Published online: 30 August 2025

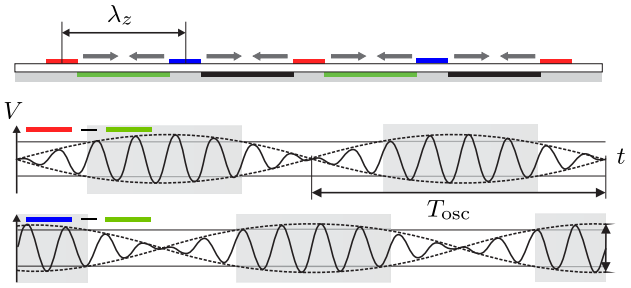

Fig. 1 Multi-electrode PA array for beat-frequency operation (Hehner et al. 2020) with color-coded electrode groups (1:●, 2:●, 3:●, 4:●) at forcing wavelength λ_z. The applied beat-frequency voltage signals over time of are illustrated for two neighboring electrode group pairs. Plasma discharges occur when the applied voltage exceeds the breakdown voltage, which is indicated as horizontal line in the sketch. The discharges cause a body force above the dielectric in alternating directions at oscillation frequency $f_{\mathrm{osc}} = 1/T_{\mathrm{osc}}$ as indicated by the horizontal gray arrows in the top drawing

four color-coded electrode groups are, respectively, supplied with sinusoidal voltage signals of identical amplitude. The concept builds upon the beat of the voltage signals between two neighboring electrode groups, resulting in potential differences that periodically exceed the breakdown voltage. The initiated phases of plasma discharges cause alternating forcing in both directions at oscillation frequency $f_{\mathrm{osc}} = 1/T_{\mathrm{osc}}$, as indicated by the arrows in Figure 1. In contrast to real wall oscillations, the spanwise forcing is periodically interrupted by the exposed electrodes, which defines the characteristic length λ_z.

Previous measurements conducted in the cross-plane above a beat-frequency-driven PA array revealed vertical motions in addition to the desired horizontally directed forcing effects and showed an increase in resulting drag in a turbulent channel flow for a first selection of forcing parameters (Hehner et al. 2022; Hehner 2022). These observations raise further questions regarding the actuator design and operation parameter choice to optimize performance. To therefore enhance the understanding of the underlying mechanisms in this highly dynamic and complex control scenario, it is crucial to explore the spatio-temporal transmission relation between plasma discharges and their forcing impact throughout the oscillation cycle further. Additionally, the forcing regularity of the used actuator arrays is to be verified as a basis for further studies of the flow control effects.

In a first step simultaneous electrical and optical measurements investigated the occurrence and characteristics of plasma discharges throughout the plasma and oscillation cycle for the beat-frequency concept by means of intensified charge-coupled device (ICCD) imaging (Pasch et al. 2023). A discrete distribution of individual plasma discharges as well as statistical illumination irregularities were observed. As a second step, aiming at investigating the fluid-mechanical momentum transfer characteristics, flow velocity and acceleration data are extracted and evaluated in the scope of this work.

Defocusing particle tracking velocimetry (DPTV) enables time-resolved, volumetric flow measurements in thin measurement volumes with comparatively simple setup, allowing to detect the flow velocity and its material derivative along pathlines directly, which makes it a promising experimental approach for the investigation of the forcing transmission behavior. In the present study, DPTV is applied to capture plasma-induced flow velocities and accelerations in a thin, wall-parallel volume directly above the actuator array in otherwise quiescent air. The tracking-based nature of the chosen measurement approach allows for a combined Lagrangian and Eulerian evaluation, enabling both, the analysis of spatially resolved flow fields as well as individual particle trajectories. This dual perspective offers complementary insights into the forcing-induced flow topology and allows for the exploration of new Lagrangian viewpoints, which represents a valuable aspect of the investigation itself. Additionally, the spatio-temporal regularity of the forcing effect is assessed based on the volumetric character of the measurements, completing the insights gained from the optical discharge characterization.

As described in detail in Section 2, calibration is a sensitive aspect of DPTV, and due to the still relatively recent and specialized nature of the measurement technique, the quantification of measurement uncertainty is of particular importance. Calibration procedures and uncertainty estimation methods for DPTV measurements applied in earlier works are mainly based on flow measurements in direct wall vicinity, which is found to be rather challenging above the PA array. Consequently, an adapted calibration procedure is implemented as an extension of an existing method, and a novel approach for a posteriori uncertainty quantification is developed for the present application. The specific limitations and introduced procedures are discussed in Sections 2.3 and 2.4. Furthermore, to address the experimental questions outlined above, continuous, i.e., time-resolved Lagrangian tracking is implemented.

The conducted experiment represents an additional benefit as a proof-of-concept experiment for future applications of DPTV for investigating the interaction of plasma-based forcing with a turbulent flow in direct wall vicinity, which has been shown to be challenging in previous works (Hehner 2022; Pasch et al. 2024), as well as wall-bounded flows, wall-near flow control applications and microfluidic flows in general.

2 Measurement technique

2.1 State of research

DPTV is based on the work of Willert and Gharib (1992) and enables to measure three-dimensional particle positions

and velocities by associating features of a defocused particle image (PI) such as shape or size with the particle position along the optical axis. Commonly applied mechanisms include astigmatism and out-of-focus imaging with and without an aperture using geometrical masks (Cierpka and Kähler 2012), out of which the latter is used here. Specifically, Fuchs et al. (2016) introduced an in situ calibrated DPTV approach for wall-bounded volumes of a few millimeters thickness, where the depth location of the tracer particle is extracted from the PI diameter. A locally adaptive intensity filter is applied for particle detection, while the PI diameter is coupled to the physical depth dimension through in situ calibration. This work forms the basis for the present measurements, as discussed later. Various alternative detection mechanisms exist in literature, such as a comparison to a calibration stack (Barnkob and Rossi 2020) or a detection via deep convolutional neural networks (Dreisbach et al. 2022).

An in situ calibrated DPTV approach was successfully applied by Leister et al. (2021, 2023a) for measurements of the oil-flow structure in an open wet clutch gap of a few hundred micrometers height. Lately, the suitability of DPTV for measurements in a turbulent channel flow (Leister et al. 2023b) and the determination of wall-near turbulent flow structures and wall shear stress in a boundary layer flow (Fuchs et al. 2023) were shown. The investigation of the plasma-based forcing effects in air imposes similar requirements on measurement techniques, especially regarding flow characteristics and the flat measurement volume shape with a high aspect ratio and the proximity to a solid wall, which is often a challenge due to background illumination effects due to scattering and reflections. As such, the chosen technique appears well-suited for application above the PA array.

2.2 Measurement principle

Figure 2 shows the measurement principle for two particles—both positioned at different distances from the camera focal plane. The diameter of their out-of-focus PIs on the camera sensor contains the explicit distance information of each particle to the focal plane. Note the intensity of the image might be several orders-of-magnitude lower, compared to an in-focus image as the same amount of light is distributed across a larger area on the camera chip. Olsen and Adrian (2000) derived a mathematical equation of this defocusing behavior under absence of optical aberration effects, which quantifies the interrelation between the PI diameter d_i on the sensor and the physical diameter size of the particle d_p as

$$d_\mathrm{i}^2 = M^2 d_\mathrm{p}^2 + 5.95(M+1)^2 \lambda^2 f_\#^2 + \frac{M^2 y^{*2} D_a^2}{(s_\mathrm{o}+y^*)^2}. \quad (1)$$

The first term describes the geometric PI with the parameter M as magnification. The second term represents the diffraction of light on the aperture, with λ as wavelength of the light and $f_\#$ as focal number of the lens. The third term describes the diameter change of d_i caused by the distance y^* of the particle to the focal plane, the opening diameter of the aperture D_a and the focal distance s_o. Figure 3a shows a graphical implementation of this equation for d_i over y^* for two

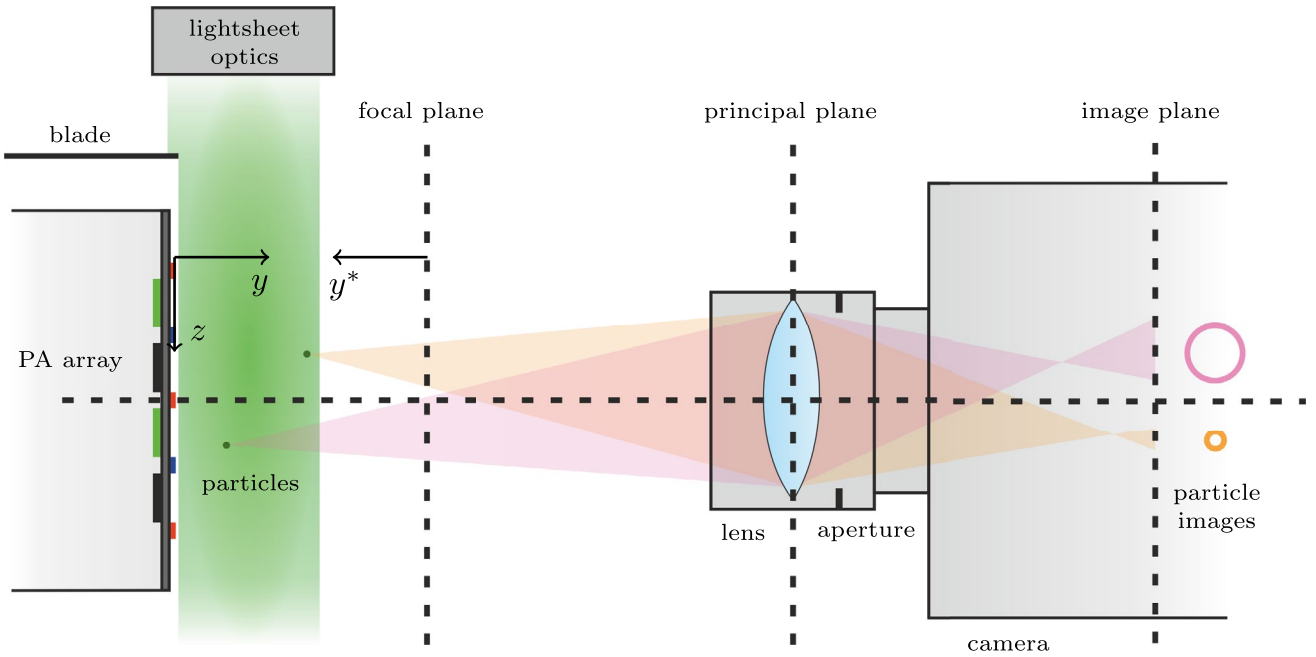

Fig. 2 Detailed, not-to-scale sketch of measurement volume above PA and DPTV measurement principle

different particle diameters d_p. With increasing y^*, the geometrical PI size and diffraction effects are not effected, while the third term, representing defocusing effects, increases. Consequently, as shown in the figure, the third term of the equation becomes the most dominant when considering particles at a specific distance from the focal plane, which applies in the current measurements. For this case, Equation (1) can be simplified to gain the linear interrelation

$$d_i = m_d y^* + d_0 \tag{2}$$

with d_0 being the PI diameter at a known position, corresponding to the wall and actuator surface in the present case. The second parameter m_d represents the slope of the defocusing function. As discussed in the upcoming subsection (Section 2.3), Equation 2 is applied as calibration function based on the calibration parameters m_d and d_0 obtained in a calibration procedure for the respective measurement setup.

2.3 Calibration

Following the in situ approach of Fuchs et al. (2016), the two parameters of Equation (2) are found empirically in a calibration procedure based on a linear fit of detected particle displacements in the near-wall flow region, identifying the particle wall diameter representing zero displacement. Depending on the experimental setup, either information at two walls (Fuchs et al. 2016; Leister et al. 2021, 2023a) is considered or the distance of the camera to a single wall (Fuchs et al. 2023; Leister et al. 2023b) is varied by means of traversing. Background illumination effects from flow-exposed surfaces make it difficult to detect particles and obtain reliable velocity data, particularly in the near-wall region. Applying DPTV directly above the PA array, i.e., the dielectric material and exposed silver electrodes, therefore, requires a modified calibration approach. To overcome these challenges, the calibration is performed in a separate step using solid particles, which are directly applied to the PA array surface. For this purpose, *Lycopodiaceae* spores are used, which are advantageous due to their known, relatively constant size of around 30 µm (Giacosa et al. 2016), providing an increased PI light intensity. The transferability of the calibration with spores to the measurements with the 1 µm Di-Ethyl-Hexyl Sebacat (DEHS) particles is feasible, as the influence of the particle diameter on the size of the PI is negligible with sufficient defocusing. This effect is shown in Figure 3a, where the PI diameter is plotted over the distance of the particle to the focal plane for particle diameters of 1 µm and 30 µm according to Equation (1). The distance range considered in the calibration and the measurement are marked in the plot in gray. Instead of evaluating PI diameters representing different wall-normal positions within the measurement volume in the calibration, the camera is moved along the optical axis as performed by Fuchs et al. (2023) and Leister et al. (2023b), while the PA array and the laser light volume can be kept stationary. For the measurement

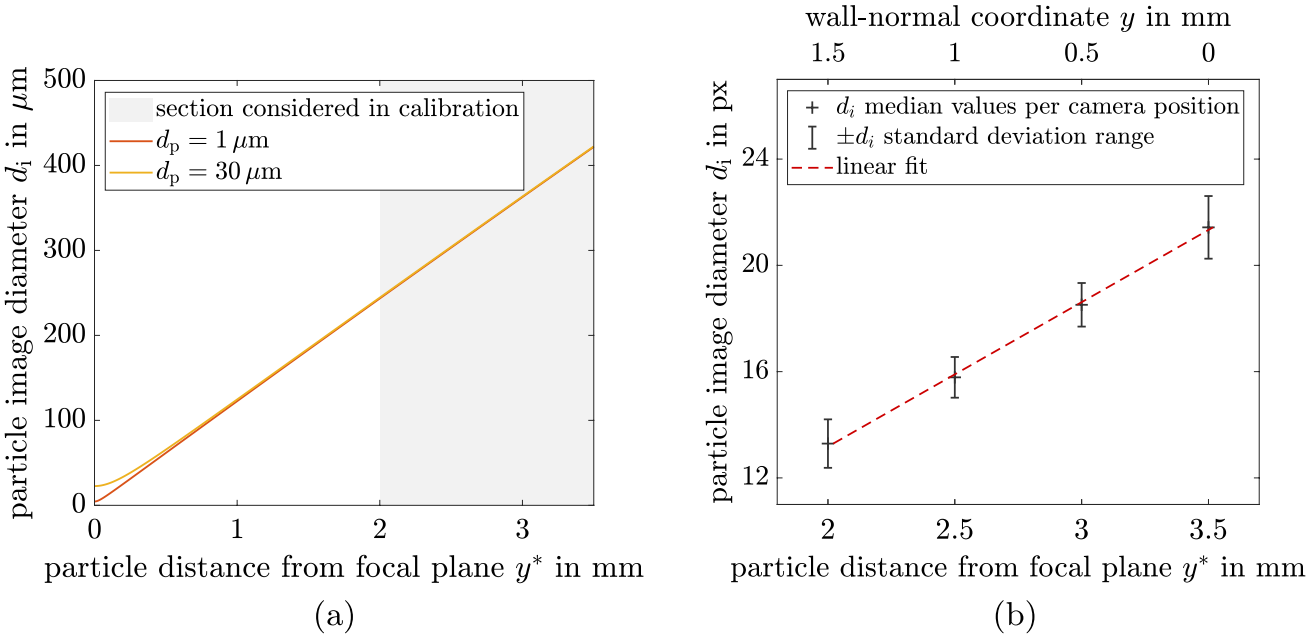

Fig. 3 **(a)** PI diameter over distance of particle from focal plane according to equation introduced by Olsen and Adrian (2000) for particle diameters of DEHS (1 µm) and Lycopodiaceae (30 µm). **(b)** Empirically determined calibration curve yielding a defocus sensitivity S^y of 184 µm/px, calibration function slope $m_d = -0.74$ px/mm and $d_0 = 7.85$ px. Note that the ordinate axes display PI diameter in different units

shown here, the respective median diameter of PIs taken at four camera positions at 0.5 mm distance from each other is evaluated to find the calibration function by means of a linear fit as shown in Figure 3b.

2.4 Uncertainty evaluation

For DPTV the spatial measurement accuracy depends on the detection of the PI diameter, in case of the out-of-plane coordinate along the optical axis, and position determination for the in-plane coordinates. Generally, a larger uncertainty is observed for the out-of-plane velocity component in previous works (e.g. Fuchs et al. 2016). In order to evaluate the measurement uncertainty quantitatively, the deviation of observed particle movement from an expected flow behavior or a theoretical solution was evaluated by Fuchs et al. (2016) and Leister et al. (2021) for the measurement of planar flows. As an alternative, Leister et al. (2023a) considered the detected particle displacement at a stationary wall, where zero displacement is assumed. The latter approach cannot be applied for the present measurements due to the challenges to measure in the immediate vicinity of the wall. Additionally, the flow above the PA array is characterized by forcing irregularities, such that the flow cannot be assumed to be planar or follow a known profile.

An alternative procedure is therefore introduced here, based on a separate measurement in which tracer particles are tracked in quasi-quiescent air at flow velocities close to 0 m/s. The measurement uses the same setup and measurement parameters as the main measurements described later on in Section 3 without the application of forcing. Over the duration of a short measurement (see Section 4 for the parameters of the here-conducted measurements), the particle movement is approximated as a straight path. The observed deviations are expected to mainly represent particle detection inaccuracies. While residual fluctuations and random motion cannot be fully avoided, they are captured in the uncertainty estimate, which therefore represents an upper bound value. The observed low average particle velocity and homogeneous velocity distribution in the measurement volume in Section 4 support the presented procedure. The standard deviation of in-plane and out-of-plane particle displacement is determined as an estimation for the velocity measurement uncertainty, which will be further discussed in Section 4.

2.5 Lagrangian tracking

In order to characterize the spatio-temporal transmission behavior of the applied forcing together with the optical and electrical footprint of the underlying plasma discharges, flow velocity and acceleration data are extracted from the measurements. For this purpose, the evaluation algorithm based on the work of Leister et al. (2021) is adapted to track individual particles in multiple consecutive frames, and the used measurement equipment and procedure (see Section 3 for details) is accordingly chosen to enable time-resolved measurements. In particular, a laser with a smaller pulse intensity and a camera with lower pixel resolution were used compared to the previous work of Leister et al. (2021, 2023a, 2023b) to enable the required increased operation frequencies at the price of reduced signal-to-noise-ratios (SNR). Consequently, continuous Lagrangian particle tracks can be detected and the fluid acceleration can be determined if two particle velocities or, respectively, three particle positions are evaluated.

3 Experimental setup and procedure

3.1 Plasma actuator construction and operation

The used PA array depicted in Figure 4a comprises five upper electrodes, each 1 mm wide, and four lower electrodes, each 3 mm wide, resulting in a total of eight discharge zones and a wavelength λ_z of 4 mm (compare Figure 1). To fabricate the upper electrodes, a conductive silver paint (sourced from *Holland Shielding Systems BV*) is applied to a polyethylene terephthalate (PET) foil, acting as a dielectric, using an airbrush pistol and a laser-cut adhesive stencil foil. Unlike for the shown actuator, the lower electrodes are made out of copper tape here instead of sprayed silver. In order to isolate the lower electrodes, a layer of polymer resin (specifically, *R&G 888658 HT2*) is encased within a 3D-printed frame, which is glued to the PET foil. Copper tape serves as the electrical connections for the PA. The upper high-voltage (HV) electrode groups (shown in blue and red in Figure 1) are supplied by two Minipuls 1 HV transformers and the encapsulated electrodes (illustrated in green and back) are supplied by two Minipuls 2 HV transformers. The plasma frequencies applied to the upper electrode groups is $f_{ac,12} = 16$ kHz and to the lower encapsulated electrode groups $f_{ac,34} = 15.949$ kHz, yielding a beat and oscillation frequency of $f_{osc} = 51$ Hz. Voltage, current and trigger signals are captured simultaneously to the DPTV measurements, enabling the assignment of the exact phase within the plasma cycle of each measurement. The equipment for the plasma generation and the electrical measurements is accommodated on the left side of the optical table that accommodates the test rig and damps possible vibrations as shown in Figure 4b.

Figure 5 shows the course of measured voltages ΔV_{13} and ΔV_{14} applied to the respective electrode groups, illustrating the beat-driven oscillation of voltage amplitude introduced in the schematic in Figure 1. Note that the envelope voltages ΔV_{24} and ΔV_{23} (not shown in the figure) are in phase

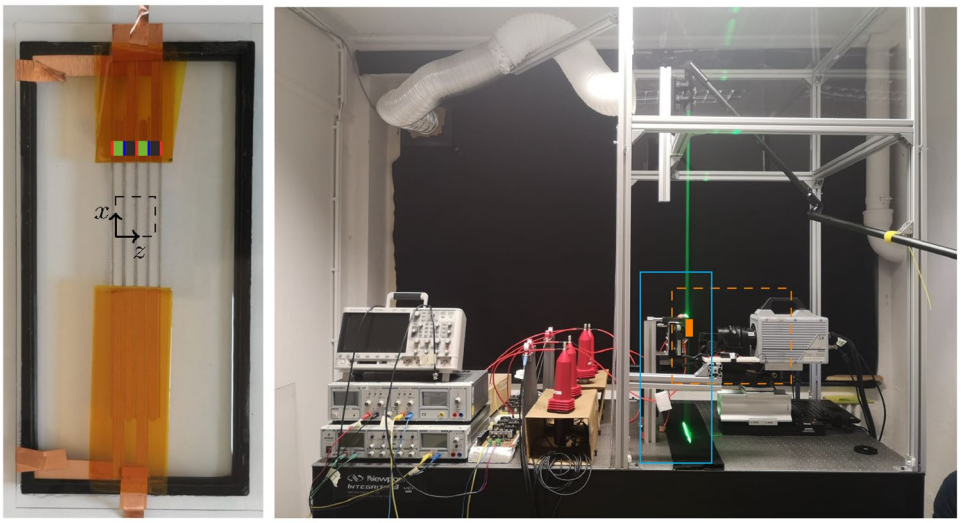

Fig. 4 **(a)** Detailed view of a similar PA array. The electrodes are shown by the color-coded blocks according to Figure 1 and the camera field of view is marked by the dashed line. Note that the array is mounted with the x-axis oriented horizontally and the z-axis vertically, so that the coordinate system is rotated in following figures. **(b)** Measurement setup comprising DC power supplies, HV transformers, coils for current measurements, HV probes for voltage measurement (left table side) and laser light sheet optics, camera, PA array (right table side). The small filled orange box shows the MV position and the larger dashed orange box indicates the immediately surrounding area comprising the optical components shown in the technical sketch in Figure 2. The framework on the right side of the table is connected to an extractor hood and can be closed with Plexiglass walls. A smaller box was inserted to shield the measurement area against influence of ambient air, which is indicated by the blue box

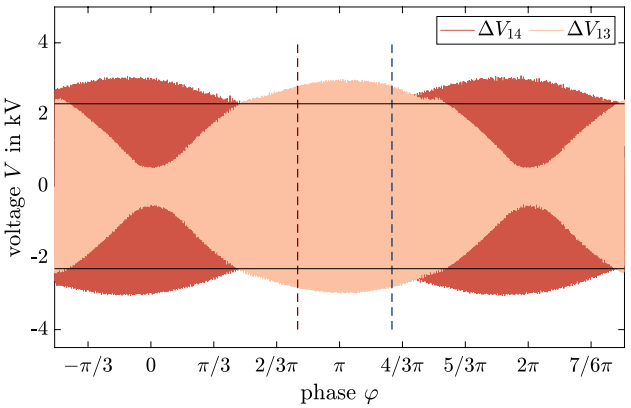

Fig. 5 Applied voltages ΔV_{13} and ΔV_{14} between upper electrode group 1 (●) and lower electrode groups 3 (●) and 4 (●) over oscillation cycle phase φ measured during the experiment. Dashed lines mark the oscillation phases $\varphi = 0.78\pi$ (red) and $\varphi = 1.28\pi$ (blue), and black horizontal lines show the breakdown voltage

with ΔV_{13} and ΔV_{14}, respectively. Accordingly, all particle positions along a detected 3D trajectory can be assigned a phase φ between 0 and 2π within the forcing oscillation cycle based on their frame of detection and the simultaneously conducted electrical measurements. Due to the strict periodicity of the forcing and its synchronization with the camera acquisition, this phase assignment is repeatable across cycles. The reference phase $\varphi = 0$ is defined as the phase of minimum peak-to-peak voltage between electrode groups 1 and 3 which corresponds to the maximum peak-to-peak voltage between electrode groups 1 and 4. This enables the construction of phase-averaged velocity and acceleration fields by grouping data from multiple cycles.

3.2 Mechanical and optical setup

The DPTV measurement setup illustrated in detail in Figure 2 is positioned on the right side of the optical table shown in Figure 4b inside an extractor hood for the removal of the applied DEHS tracer particles (1 µm diameter (Raffel et al. 2018), Stokes number $\mathrm{Stk} \approx 1,5 \times 10^{-3}$) and generated ozone. An additional, smaller Plexiglas box, which is not shown in the figure, with an opening on the side facing the camera is positioned around the PA to reduce the influence of external air flow in the room on the measurement results. The PA array is attached to a vertical mounting platform with precision screws for fine adjustment of the pitch angle and horizontal position. The laser beam enters the measuring chamber via a mirror arm and is expanded using light sheet optics with an 8° cylindrical lens. The resulting laser light volume is positioned parallel to the PA array, with in-plane expansion in the x and z directions being much larger than the thickness in the y direction, yielding a measurement

volume size of 14 mm × 1 mm ×14 mm in x, y and z direction. A horizontal blade is inserted above the PA mounting platform and can be fine-adjusted in y direction to align the laser volume with the actuator surface.

A Nd:YLF laser with a wavelength of $\lambda = 527$ nm and a pulse width of < 210 ns is operated in double-pulse mode. To increase the illumination intensity for the measurements, both laser cavities are fired simultaneously rather than in alternating sequence at a constant pulse frequency of 1837 Hz (corresponding to a pulse distance of $\Delta t = 544.270$ µs), resolving the oscillation cycle in 36 phases. The camera is positioned opposite the PA array using an electrical fine traverse for horizontal adjustment of the distance. An adjustment screw for the PA array yaw orientation allows to align the actuator surface with the optical axis of the camera. The focal plane is positioned approximately 3.5 mm in front of the PA array, causing particles closer to the actuator to appear more defocused and accordingly larger. The camera (evaluated sensor section size of 512 × 512 pixel, 12 bit resolution) is equipped with a $f = 50$ mm lens at $f_{\#} = 2$ aperture, and an additional distance ring of 12 mm. The measurements are taken at a magnification of 0.74, yielding a reproduction scale of S^{xz} of 27 µm/px. Table 1 provides a detailed list of model specifications and corresponding manufacturers for the used components.

A parameter study is conducted to optimize the setup, balancing surface illumination effects due to scattering and reflections and the shielding of particle illumination near the wall. Therefore, the light sheet optics distance from the actuator in the negative z direction (and, thus, the light volume width in the measurement volume) and the y position of the blade cutting the light sheet are systematically varied. The camera-to-PA distance is maintained constant to ensure a consistent defocusing level. Additionally, the PA array surface is coated with a thin black layer applied by a brush pen to reduce background illumination effects due to scattered and reflected laser light.

4 Results and discussion

4.1 Image processing and particle tracking

Before detecting and tracking individual PIs, a pre-processing routine illustrated in Figure 6 is applied to enhance the SNR and reduce background illumination artifacts from dust and the borders of the upper electrodes which occur when laser light reaches the PA surface. This is caused by diffraction of the light around the knife edge, beam divergence effects and the light intensity distribution within the light volume, despite the careful adjustment of the setup components described in Section 3.2. First, a background image is subtracted, generated from a moving median of consecutive frames. Note that the number of frames considered is aligned with the velocity-dependent

Table 1 Components used in the experimental setup sorted by subsystems

Setup component	Device and manufacturer
Plasma generation	
Function generator	Synchronizer control unit *ILA 5150 GmbH*
Power Supply	VLP-2403 Pro, VSP-2410, *VOLTCRAFT*
HV transformer	2 × Minipuls 1, 2 × Minipuls 2, *GBS Elektronik GmbH*
Electrical measurements	
Oscilloscope	Picoscope 4424, *Pico Technology Ltd.*
HV probes	Pintek HVP-39pro, *Pintek Electronics Co., Ltd.*
Current transformer	Magnelab CT-C1.0 Rogowski coil, *Magnelab Inc.*
Optical measurements	
Laser	Darwin-Duo 527-100-M *Quantronix Corp.*, energy per puls: 60 mJ
Laser beam propagation	Articulated Mirror Arm *ILA 5150 GmbH*
Light sheet optics	Standard Light Sheet Optics with cylindrical lens with effective focal length of 125 mm *ILA 5150 GmbH*
Lens	*Zeiss* $f = 50$ mm, $f^{\#} = 2$ and 12 mm distance ring
Camera	FASTCAM SA4, *Photron Deutschland GmbH*, pixel size: 20 µm × 20 µm
Seeding particles	DEHS
Seeding generator	PIVlight30 *PIVTEC GmbH*
Mechanical equipment	
Traverse system for camera	Linear Translation Stage w. Integrated Controller, Stepper Motor *Thorlabs, Inc.*
Vibration damping	Optical table M-INT3 series *Newport Corporation*

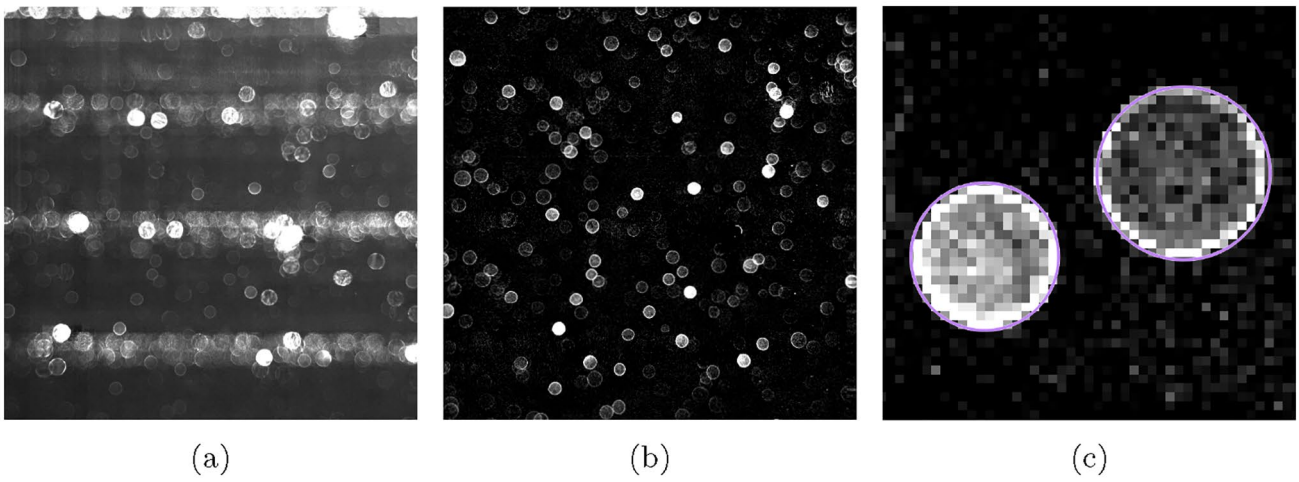

Fig. 6 Illustration of image pre-processing and processing routine: **(a)** raw image, **(b)** image after background subtraction and contrast enhancement, **(c)** zoomed-in view of image section with two PIs with purple visualizes of the result of the PI recognition using the Hough transform

particle displacement in-between frames to avoid the removal of slow particles. The so-generated background images are weighted by the instantaneous illumination level of each frame. A contrast enhancement is then applied to further improve the images.

For the flow measurements, the average PI pixel illumination is approximately 254 counts and the illumination of the brightest pixels of a PI 614 counts (12-bit depth, maximum count 4096), depending on local illumination and in-depth particle position, which was partly exceeded by the intensity of background artifacts from the electrodes. The average image intensity of an exemplary raw image for the given experimental settings was at 216 counts, resulting in a typical SNR for the brightest pixels of a PI of approximately 2.8. After applying the pre-processing, the visibility of the PIs and their contrast to the background are clearly enhanced.

As a next step, the PI positions and diameters are identified for each individual image. The procedure and implementation for the PI recognition are based on the Hough transform (Hough 1959), as implemented in the MATLAB function *imfindcircles*. An example for the detected circles for two PIs is shown in Figure 6c. For the implementation of Lagrangian DPTV, a tracking algorithm for the reconstruction of particle motion across multiple frames is developed, generating trajectories of varying lengths.

Velocity values are based on the particle displacement between two consecutive frames as $\vec{u} = \Delta\vec{x}/\Delta t$. Two successive particle displacements, or correspondingly three particle positions, result in one acceleration value $\vec{a} = \Delta\vec{u}/\Delta t$. In order to assign velocity and acceleration values to a given phase within the oscillation cycle, a symmetric set of five consecutive particle positions along a time-resolved track, corresponding to four velocity and three acceleration values is used.

The particle recognition and tracking algorithms are based on the methods used by Leister et al. (2021). For each PI that is detected in one frame, a search is conducted in the subsequent frame within a defined maximum displacement range, similar to a nearest-neighbor approach. The expected displacement range is adjusted iteratively to the given flow and therefore chosen smaller for the quiescent air measurements than for the main experiments. If a match is found, the respective 3D particle position is added to the track. The process is then repeated for the next frame. The track terminates if no suitable PI is found or if multiple potential matches are detected. The outcome of this approach is the generation of trajectories of varying lengths. The procedure is performed for all PIs in all frames that are not assigned yet to a track starting in previous frames.

4.2 Measurement uncertainty analysis

As described in Section 2, a new approach has been developed to evaluate the measurement uncertainty for the present experiment. In order to reduce air movement due to the influence of ambient air, the test-rig housing is closed and then allowed to rest for several minutes before the measurements are carried out. While the procedure is found to improve the conditions for the presented uncertainty estimation approach, perfectly still air conditions are not achievable. To acknowledge this limitation, the resulting state is referred to as quasi-quiescent air.

As shown in Figure 7, the particles are observed to move slowly along seemingly straight tracks in the described setting. A closer look (compare detail view of exemplary track in a volume of size 0.19 mm × 0.35 mm × 0.53 mm in x, y and z direction), however, reveals that the detected particle positions fluctuate along these linear paths. From the particle

tracks identified in the uncertainty evaluation measurement, 70 tracks with particles detected in 50 to 100 consecutive frames are evaluated.

The mean PI displacements between two frames are found to be 0.05 px in negative x direction, 0.12 px in negative z direction and the mean PI diameter change between two frames was 0.00008 px. This yields an approximate absolute flow velocity of 6.4 mm/s for the reported reproduction scale S^{xz}, the defocus sensitivity S^{y} and the temporal delay between two consecutive frames Δt.

The measurement uncertainty is estimated based on the PI displacement and diameter change standard deviations within individual particle tracks. The evaluated mean values are $\sigma_{\Delta x,\Delta z} = 0.33$ px for in-plane PI displacements and $\sigma_{\Delta y} = 0.46$ px for out-of-plane PI diameter change. Based on the reproduction scale for the in-plane displacements S^{xz} and the defocus sensitivity for out-of-plane displacements S^{y} and the temporal delay between two consecutive frames Δt, the estimated velocity measurement uncertainty yields $\sigma_{u,w} = 0.016$ m/s for in-plane motion and $\sigma_{v} = 0.156$ m/s for out-of-plane motion, while the maximum flow velocities induced by the plasma-based forcing are in the order of magnitude of 1 m/s.

The estimated measurement uncertainty, especially of the out-of-plane displacement, which is reconstructed based on the change of the PI diameter, is found to be comparably large (Fuchs et al. 2016; Leister et al. 2021). However, note that different methods were used for determination, but both would tend to overestimate the measurement uncertainty, as flow-induced deviations of fluctuations and random motions cannot be entirely avoided and are included in the value.

To investigate the observed effect further, possible influencing factors and ongoing potentials are analyzed starting from the calibration curve slope, which indicates how many different out-of-plane positions can be distinguished. A given measurement volume depth Δz is represented by a range of detectable PI diameters Δd_i, where the largest possible d_i is limited by the image intensity at which PIs can still be distinguished from camera noise and be detected. This effect is a specific issue in DPTV, since the scattered light is spread over a larger area on the camera chip when defocused stronger. Accordingly, the largest, still detectable size of PIs is majorly limited due to the physical particle size and corresponding scattering properties, as well as the available laser light intensity. It further depends on the camera-specific illumination sensitivity and noise level, as well as the lens-dependent PI shape in combination with the image evaluation algorithm. On the other hand, the evaluation of smaller PI diameters is, again, limited by the detectability of the applied image evaluation algorithms, particularly the use of the Hough transform in the present measurements. Additionally, it must also be ensured that the linearization assumption for the calibration function still applies. Considering the image evaluation algorithm, the interplay of the camera sensor physical pixel size and the image magnification is crucial for the pixel resolution of the ring-shaped PIs. Since the pixel size of 20 µm of the here-used camera is

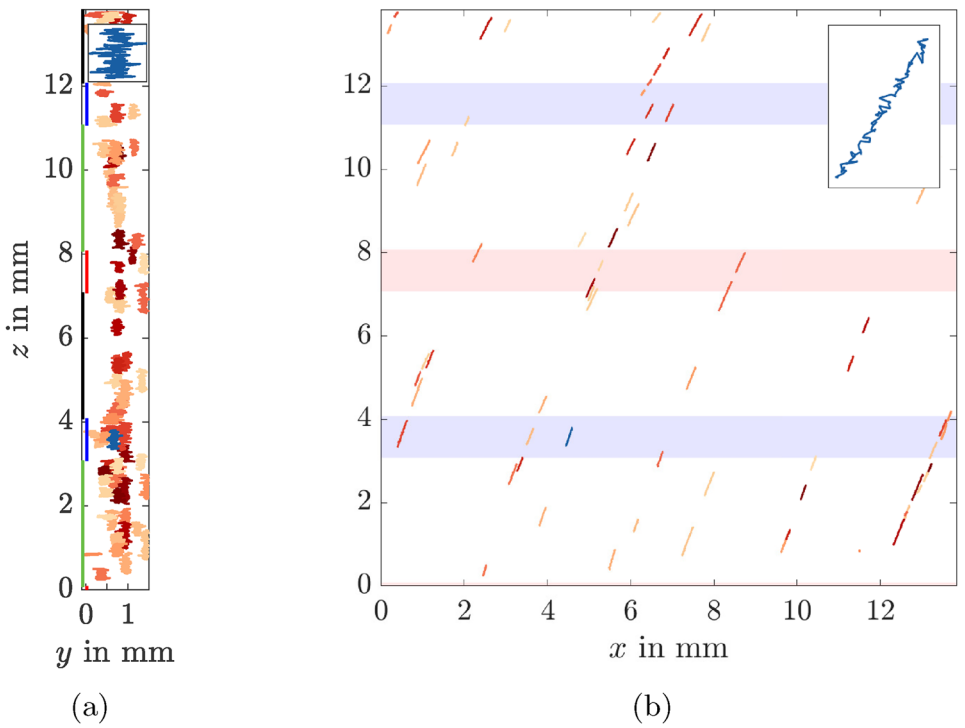

Fig. 7 Particle tracks in almost quiescent air, (a) in y-z plane, (b) in x-z plane and zoomed-in view of particle track in highlighted in blue. Colors are chosen to distinguish different tracks and indicate the information of a separate track. Electrode positions are shown for clarity, with color-coding based on electrode groups as defined in Section 1

comparatively large, the brighter PI edge is represented by fewer pixels (compare Figure 6), likely limiting the algorithm performance and PI size detection accuracy.

Consequently, several practical measures can be implemented to enhance the accuracy of DPTV measurements. Initially, the size of the measurement volume is specified by the investigated problem and the tracer particles should be sufficiently small to ensures they track the flow dynamics accurately, requiring comparably small particles for measurements in air. However, increasing the laser light intensity and applying a camera which allows for an increased sensitivity and/or SNR enhances the PI quality. A reduced camera pixel size increases resolution of PIs, providing finer information for determining their position and size when the SNR is sufficient. However, such adjustments need to be carefully balanced with the interplay of magnification, the lens-specific imaging characteristics and the performance of the applied image processing algorithms.

As shown below, the Lagrangian measurement data can be sorted onto a spatial grid by means of local averaging, enabling the construction of velocity and acceleration fields. This spatial organization allows the application of a different statistical approach to express the uncertainty of a bin-averaged quantity $\bar{x}$, called the standard error of the mean (Altman and Bland 2005) which is given by

$$\sigma_{\bar{x}} = \sigma/\sqrt{N} \tag{3}$$

with standard deviation σ and sample size N. The standard error of the mean represents the uncertainty in this context because the values within each bin are derived from multiple independent samples, providing a more robust estimate of the field's statistical uncertainty.

The corresponding values for the present experiment, listed in Table 2, are based on a binning procedure and applied field resolutions that will be introduced later with a minimum of $N = 25$ or $N = 40$ samples per bin, respectively. The standard error of the mean for in-plane displacements $\sigma_{\overline{\Delta x,\Delta z}}$ is based on the PI position uncertainty $\sigma_{\Delta x,\Delta z}$ and the reproduction scale S^{xz}. For the standard error of the mean for out-of-plane displacements $\sigma_{\overline{\Delta y}}$, the out-of-plane displacement uncertainty $\sigma_{\Delta y}$ and the defocus sensitivity S^{y} are evaluated. It is shown that the uncertainty of the averaged quantities induced by the measurement technique is in the order of magnitude of only 1 to 20 µm for the chosen grid cell sizes specified below.

Table 2 Standard error of the mean for in-plane and out-of-plane displacement between two consecutive frames for sample size $N = 25, 40$

N	$\sigma_{\overline{\Delta x,\Delta z}}$ in µm	$\sigma_{\overline{\Delta y}}$ in µm
25	1.78	16.93
40	1.41	13.38

4.3 Flow topology

Based on the experimental setup and methods described in the previous sections, velocity and acceleration data along individual particle tracks were detected above the PA array. In total, approximately 43 000 images representing 1200 oscillation cycles were evaluated, yielding 190 000 particle tracks. On average, 40 particles were detected in each image, yielding a PI density (also referred to as source density N_S) of 0.036 based on the ratio between the sum of PI areas and the full image area (Barnkob and Rossi 2020; Cierpka and Kähler 2012).

It is important to note that the determined acceleration from the Lagrangian tracks represents the material acceleration experienced by the individual particles, i.e., $\vec{a} = \Delta\vec{u}/\Delta t = \mathrm{D}\vec{u}/\mathrm{D}t$. If multiplied with a density ϱ this term states the left-hand side of the momentum equation without any requirements of spatial derivatives for the convective term. Accordingly, the determined acceleration $\vec{a}$ automatically provides immediate insight into the sum of specific forces $\sum \vec{F}/\varrho$. For the case of steady PA operation in quiescent air, this sum has been demonstrated to be predominated by the applied PA-based body force, i.e., $\sum \vec{F}/\varrho \approx \vec{f}_{\mathrm{bf}}$ (see, e.g., Kriegseis et al. 2013; Benard et al. 2013). As such, the below discussion on acceleration in turn also indicates a valuable spatio-temporal footprint of the applied body force to the observed flow topology.

4.3.1 Lagrangian particle tracks

Figure 8a and 8b shows 500 and 3000 exemplary tracks color-coded according to their local acceleration a_z in the y-z plane and x-z plane, respectively. In accordance with the expected effect of the plasma-based forcing and earlier investigations (Hehner et al. 2020), the particle movement is observed to mainly occur in z direction, perpendicular to the electrodes. The figures clearly show that particles experience high acceleration close to the wall above the lower electrodes and next to the, respectively, involved upper electrodes, where the strongest forcing effect of the PA is located. In this context, the regions of maximum accelerations in positive and negative z direction occurring throughout the oscillation cycle, represented by the red and blue color-coding, do not perfectly overlap but are instead shifted to different z positions. The figure visualizes the local density of particle detection decreasing near the wall and especially above the upper electrodes, likely due to increasing PI size at larger distances from the focal plane and background illumination effects especially above the exposed silver electrodes exceeding the dielectric surface. Despite this irregularity in spatial particle detection

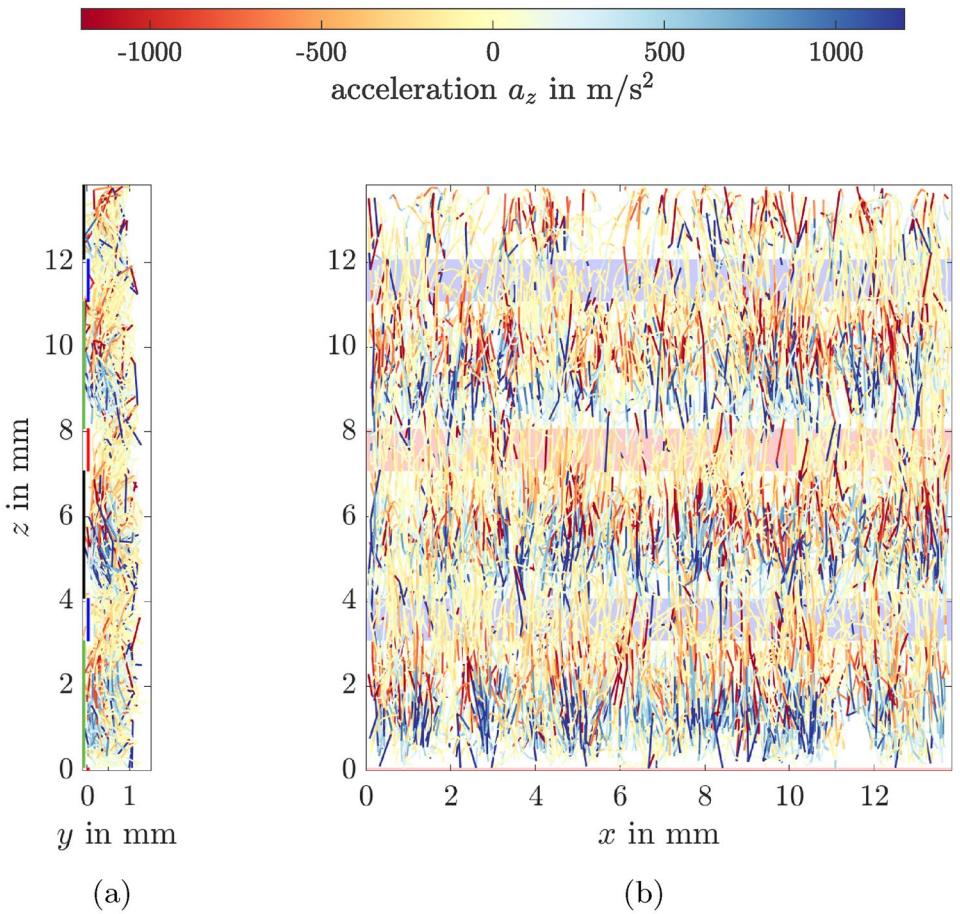

Fig. 8 Particle tracks under oscillating forcing (a) in y-z plane, (b) in x-z plane color-coded according to their z acceleration. Electrode positions are shown for clarity, with color-coding based on electrode groups as defined in Section 1

distribution, it is shown that particles were generally found over the entire measurement volume, proofing suitability of DPTV measurement technique and the chosen setup for an investigation of the plasma-induced flow directly above the wall.

In the following, a closer look is taken at the paths of individual particles. 40 tracks are considered that pass the same z position range between $z = 5$ mm and $z = 6$ mm in the chosen coordinate system during the same oscillation cycle phases $\varphi = 0.78\pi$ and $\varphi = 1.28\pi$, respectively, corresponding to phases 14 and 23 out of 36. The spatial range represents the center region above one of the encapsulated electrodes, where maximum cumulative forcing impact is expected throughout the oscillation cycle. The phases are 1/4 of the oscillation cycle apart from each other and arranged symmetrically around the phase of maximum voltage as marked in the voltage diagram in Figure 5 with vertical dashed lines. The particle tracks representing these phases are shown in Figure 9a in red and blue shades, where the intensity gradient indicates the progression of time or, correspondingly, direction of movement from light to dark. The potential differences ΔV_{13} and correspondingly also ΔV_{24} increase during phase $\varphi = 0.78\pi$, reach their maximum shortly after and decrease again during phase $\varphi = 1.28\pi$. Thus, the considered phases are associated with forcing in positive z direction. In accordance with this, it can be observed that most red particle tracks starting in phase $\varphi = 0.78\pi$ reverse from negative to positive z direction during the first frames of observation. Most particle tracks marked in blue move predominantly in positive z direction in phase $\varphi = 1.28\pi$ and the upcoming frames, while a change of direction can be observed in later frames of the longest particle tracks.

The reversal of the direction of particle movement is often accompanied by a seemingly non-systematic lateral drift in x direction. This may indicate an instability in the movement when the z velocity component becomes very small, potentially caused by superimposed convective effects near the actuator caused by forcing distribution irregularities or wavering of the surrounding air. At the same time, most observed particles of both starting phases experience a downward movement in negative y direction, which is not visible in the shown topview perspective.

Generally, tracks passing through the same volume during the same oscillation phase resemble each other, indicating coherent forcing-based flow behavior. However, the Lagrangian perspective allows the evaluation of individual events and their deviations, which would otherwise only occur in

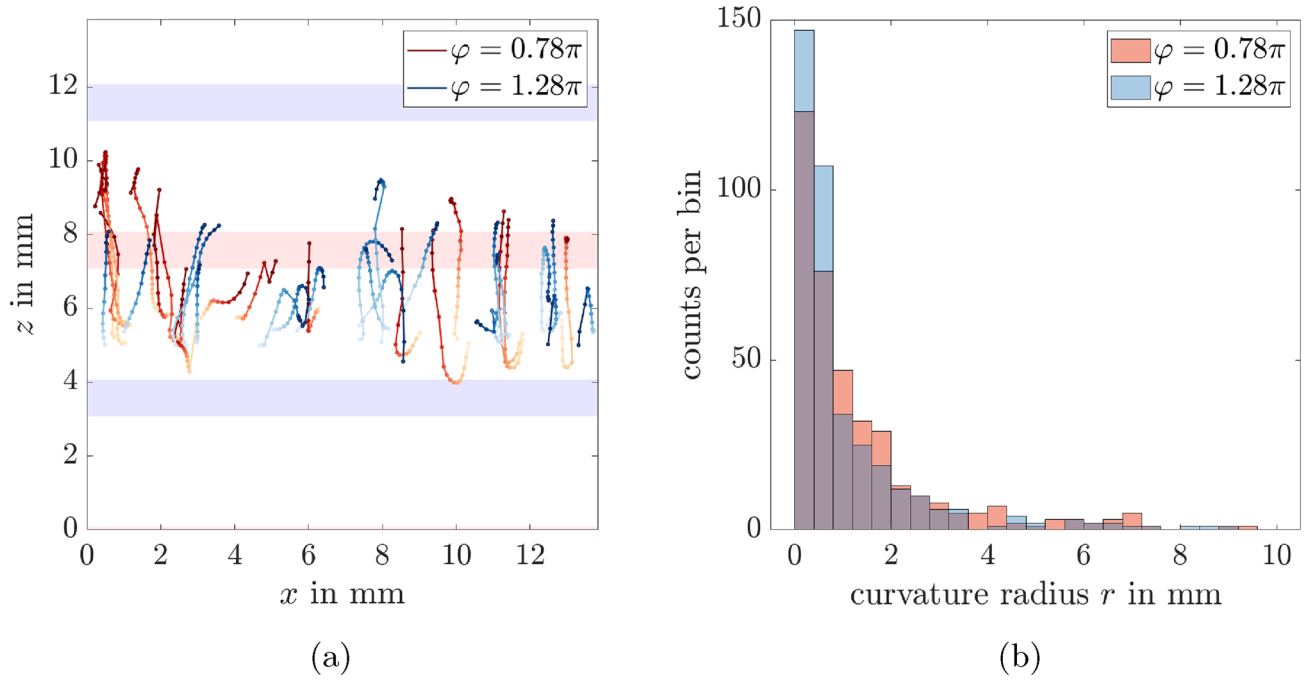

Fig. 9 **(a)** Particle tracks in the x-z plane which have crossed z-positions between $z = 5$ mm and 6 mm during the same oscillation phases $\varphi = 0.78\pi$ (red) and $\varphi = 1.28\pi$ (blue). Color gradient indicates particle direction from light to dark shade of color. Electrode positions are shown for clarity, with color-coding based on electrode groups as defined in Section 1. **(b)** Histograms of particle track curvature radii $r = 1/\kappa$ according to Equation (4) in the y-z plane determined from tracks passing the same volume in oscillation phases $\varphi = 0.78\pi$ (red) and $\varphi = 1.28\pi$ (blue)

statistical flow quantities. Thus, a physical interpretation of individual particle behavior and, on this basis, a distinction of flow-driven events and measurement noise are possible. Braun et al. (2006) identify the curvature of a particle path given by

$$\kappa = \frac{1}{r} = \frac{|\vec{u} \times \vec{a}|}{|\vec{u}|^3}, \tag{4}$$

as one aspect for the intrinsic geometric characterization of a curve in 3D space, where r is the respective curvature radius.

Figure 9b shows histograms of, respectively, 400 curvature radii values observed within the considered tracks. Note that for this evaluation only the curvature in the y-z plane is considered to avoid any possible impact of the afore discussed drifts occurring in x direction. It is observed that within tracks passing the same z range at earlier oscillation cycle phase $\varphi = 0.78\pi$ (red) the radii tend to be slightly larger than for those passing at $\varphi = 1.28\pi$ (blue). The effect can be associated with the temporal evolution of vortical structures over the course of the oscillation cycle, which result from the forcing-induced motion in z direction and superimposed downward motion toward the electrodes, leading to the formation of vortex structures of varying expansion at different phases.

These results highlight the effectiveness of the Lagrangian measurement approach in accessing topological features—such as the formation of vortical structures—from spatially sparse data, where Eulerian field information would suffer from coarse spatial (discretized) resolution. Particularly, the particle track curvature provides a quantitative measure for characterizing vortical motions as a result from the PA force. This allows individual particle tracks to be compared or grouped based on flow features, helping to organize and better understand complex flow patterns directly from the particle motion.

In summary, particle tracks are detected over the entire measurement volume, demonstrating the suitability of DPTV for near-wall flow measurements above the PA. The extracted velocity and acceleration values characterize the particle motion throughout the oscillation cycle, showing the formation of vortical structures and a spatial decoupling of acceleration zones toward both directions for the present geometrical actuator parameters. At the reversal of the forcing direction a tendency of the particles is observed to laterally drift in the x direction along the electrodes. The evaluation of Lagrangian tracks is shown to offer an analysis of individual flow events and their coherence, offering new insights for the identification and interpretation of topological features.

4.3.2 Extracted Eulerian flow fields

In a next step, the captured flow data are projected on a grid by calculating mean velocity values within each grid cell. The Eulerian perspective allows a statistical evaluation of the observed particle tracks in order to link the flow data to the above-mentioned electrical–optical measurements (Pasch et al. 2023).

The applied particle tracking algorithm requires a low particle density, yielding sparse instantaneous data. The binning is based on a phase-averaging approach aligned with the cyclic character of the oscillating flow forcing. Accordingly, all values assigned to the same grid cell and phase are averaged, resulting in near-continuous, volumetric, phase-resolved velocity and acceleration fields. As applied in the later evaluations, the spatial grid and phase resolution of the binning allow to display the measurement results from different perspectives, demonstrating the flexibility achieved through the Lagrangian measurement approach with the measurement time and corresponding data statistics being the limiting factor. Accordingly, the local data density needs to be considered, which depends on the illumination distribution, imaging effects and the algorithm performance. As already discussed above, the statistical convergence of averaged data depends on the measurement noise as well as the deviation of occurring physical events.

First, the measurement volume is divided into 15 bins in y and 40 bins in z direction, yielding respective spatial resolutions of 0.1 mm and 0.35 mm. No partition of the measurement volume in x direction is considered, as the forcing is applied continuously along this direction. A velocity or acceleration value is assigned to a grid cell when at least 40 data points were detected in the respective cell, which is determined empirically to allow for statistical convergence of the mean values. The expected displacement uncertainty based on the measurement technique is given in Table 2. Figure 10 shows the z-component acceleration distribution in the y-z plane as contour plot and the in-plane velocity fields as vector arrows for six out of 36 phases within the oscillation cycle.

Flow fields in the x-z plane are shown in Figure 11, where the same procedure is applied for a grid with 14 cells in x and z direction and a corresponding spatial resolution of approximately 1 mm in both directions. Different from the approach above, the shown flow field represents only the lower third of the measurement volume from the PA array up to 500 µm above it, as the flow field is known to deviate strongly along the wall-normal direction (compare Figure 10). For this choice of spatial resolution the total number of grid cells increases, while less particle track data are considered in the binning. At the same time, a large velocity gradient occurs in wall-normal direction. To yield a mostly continuous flow field representing the near-wall flow layer the minimum number of values per grid cell is reduced to 25. These aspects are considered in the interpretation of the flow fields.

The surface plots in Figure 10 show that particles experience high acceleration in horizontal direction in the region above the encapsulated electrodes on the side of the, respectively, involved upper electrodes due to the plasma-based forcing. Subsequently, deceleration is observed further downstream along z, where the particle velocity decreases again (compare phases 1 and 3 in Figures 10 and 11, respectively). The maximum occurring flow velocities are in the order of magnitude of 1 m/s, with the maximum acceleration being around 1000 m/s^2. Over the course of one oscillation cycle, the forcing strength toward one direction can be observed to increase, e.g., between $\varphi = 2/3\pi$ and $\varphi = \pi$, and then decrease, e.g., between $\varphi = \pi$ and $\varphi = 4/3\pi$. Eventually, the forcing in opposite direction begins, as visible in phase $\varphi = 5/3\pi$ and the reverse process takes place. The velocity field that develops under the influence of the described oscillating forcing indicated by the quiver plot is predominantly horizontally oriented. The flow direction is observed to reverse shortly after the forcing direction changes. The average flow velocities in x direction in Figure 11 are mostly very small, indicating that the drift events at flow direction reversal in Figure 9a cancel out statistically and do not represent dominant local flow structures. In addition to the desired horizontal flow, a downward motion can be observed above the regions of strongest forcing, which induce the already mentioned vortical flow structures. These can be associated with a potential increase in skin friction drag, since high-momentum fluid is pulled toward the wall in these structures in a (turbulent) shear flow.

Both perspectives on the plasma-induced flow fields in Figures 10 and 11 emphasize the symmetric character of the forcing throughout the oscillation cycle. In particular, the phases opposite to each other in the oscillation cycle, separated by $\Delta\varphi = \pi$, exhibit phenomenologically similar yet oppositely oriented behavior. This indicates that the applied voltages are balanced and the actuator geometry is manufactured with sufficient precision, which are important requirements for the development of the plasma-based implementation of the oscillating wall effects. Small irregularities can for example be observed in phase $\varphi = 1/3\pi$, where the forcing effect is stronger between the electrode groups marked in red and black than those shown in green and blue. A study of forcing homogeneity along electrodes is limited by the achieved resolution in x and z direction in the context of statistical convergence of the data shown in Figure 11 especially near the wall for the reasons discussed above. However, some local deviations are indicated, e.g., in the acceleration field shown for phase $\varphi = 5/3\pi$ in the region of z between 5 and 7 mm.

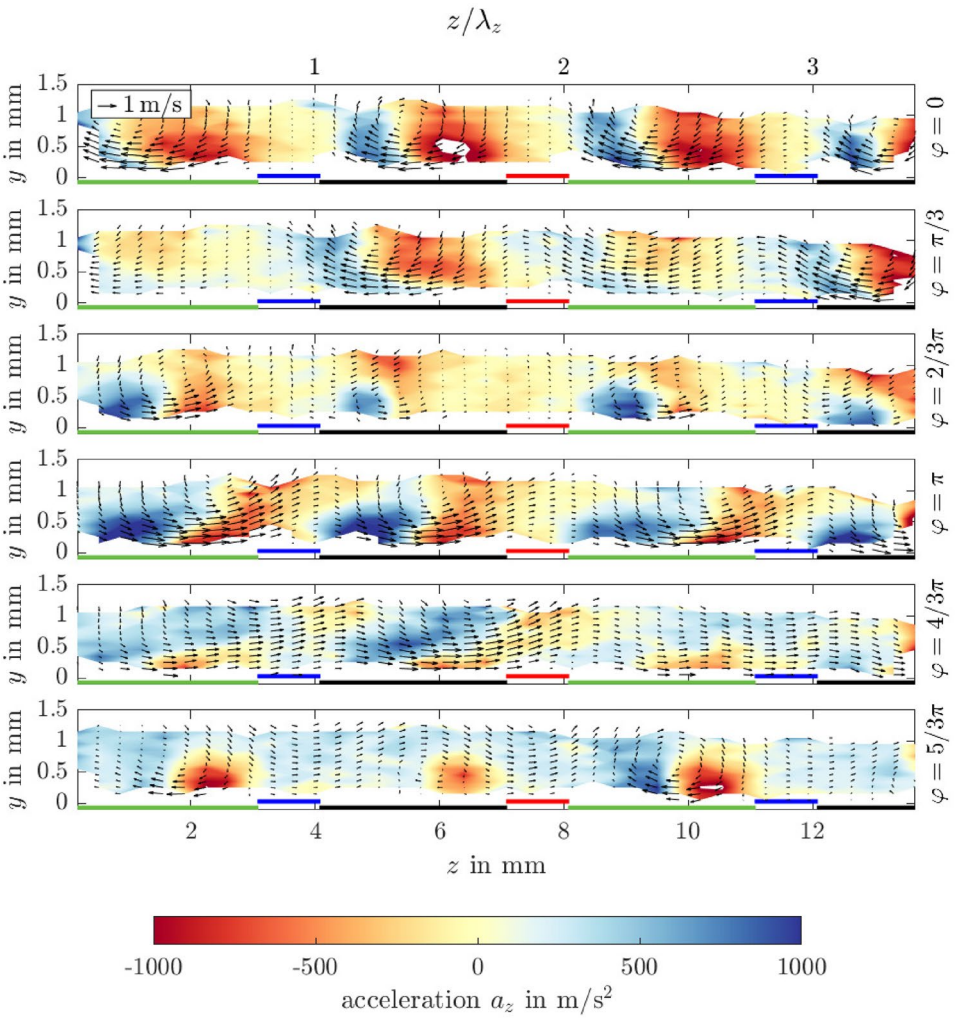

Fig. 10 Distribution of z acceleration as surface plot and in-plane velocity as quiver plot in y-z plane for six exemplary oscillation phases. More intense shades of colors indicate higher z acceleration. Electrode positions are shown for clarity, with color-coding based on electrode groups as defined in Section 1. A scale vector representing $w = 1$ m/s is added as reference

The presented results demonstrate that phase-resolved, nearly continuous, volumetric Eulerian velocity and acceleration fields can be derived from the instantaneously, rather sparse particle tracks captured using DPTV. The spatial grid resolution can be adjusted flexibly, allowing to focus on different aspects on the flow, though it remains constrained by the statistical convergence at the available data density. It is shown that the particles experience a strong acceleration near the edge of the upper electrodes and decelerate further downstream before the subsequent upper electrode. The periodically regular formation of vortical structures, characterized by downward motion toward regions of strong forcing and upward motion thereafter, is observed. Compared to the Lagrangian perspective, the Eulerian field data offer a more statistical representation of the flow above the oscillating PA array, enabling an evaluation of the forcing regularity and homogeneity. A regular distribution of velocity and acceleration along multiple discharge zones, as well as symmetrical behavior of opposing discharge zones, is observed. Despite minor local deviations, these findings support a good balance of applied voltages for the electrode groups and sufficient manufacturing precision.

4.3.3 Interplay of acceleration and velocity

In order to investigate the spatio-temporal transmission behavior of the plasma-based oscillating forcing from a quantitative perspective, the relation between velocity and acceleration fields is investigated. As a measure for the respective footprints in the flow, the mean of velocity and acceleration profiles shown in Figure 10 is considered in wall-normal direction up to 0.7 mm. The respective mean values over the spanwise z direction and oscillation cycle phase φ are illustrated in Figure 12 as surface and contour plots for velocity u_z and acceleration a_z, respectively.

The distribution of mean acceleration values over z for phases between approximately $\varphi = 0.5\pi$ and $\varphi = 1.5\pi$ shows well how the flow is accelerated by the forcing in the region next to the upper electrode in shades of blue and decelerated further downstream in positive z direction in shades of red.

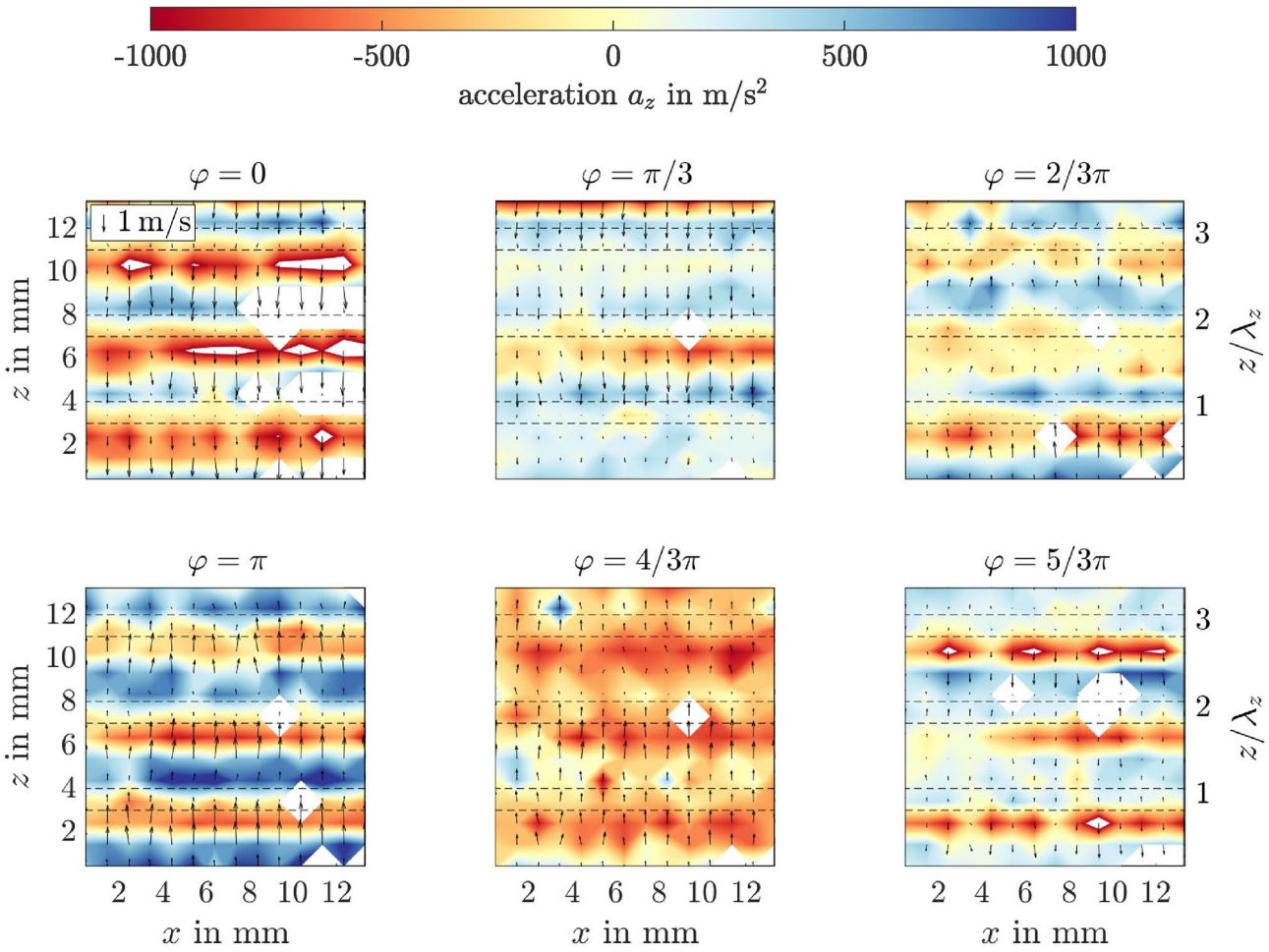

Fig. 11 Distribution of z acceleration a_z as surface plot and in-plane velocity as quiver plot in x-z plane representing the velocity data detected in a 500 µm thick volume above the PA array for six exemplary oscillation phases. More intense shades of colors indicate higher z acceleration. Electrode positions are indicated with dashed lines for clarity. A scale vector representing $w = 1$ m/s is added as reference

The z extension of high acceleration values is shown to first increase gradually over the phase and then decrease more abruptly when the forcing direction changes. The acceleration strength increases and decreases evenly over the phases with the maximum value approximately in the middle of the forcing period at potential difference peaks $\varphi = \pi$, where the applied voltage amplitude is at its maximum (compare Figure 5). The mean velocity distribution reveals a similar spatio-temporal pattern as the forcing-based acceleration distribution but appears shifted in space and time. As such, the maximum mean velocity value is located approximately 1 mm downstream in z direction and $1/6\pi$ later within the oscillation cycle, being equivalent to $1/4\lambda_z$ and $1/12T_{\mathrm{osc}}$, quantifying the convective shift and inertial delay of the flow response to local acceleration. Similar effects are observed for the opposite forcing direction across the other phases of the oscillation cycle.

The temporal evolution of the oscillatory flow pattern along z, in contrast, can be related to the rate of change of the estimated plasma length Δz_{bf} (which is the momentum transfer length, compare Kriegseis et al. 2013) on the dielectric, i.e., $\partial \Delta z_{\mathrm{bf}}/\partial t$, which is known to increase with increasing voltage amplitude (Benard and Moreau 2014; Kriegseis et al. 2016). This term corresponds to the inverse of the slope $\partial\varphi/\partial z$ in the interplay map of Figure 12, which is particularly salient in the range around $\varphi = \pi$ separating the force-driven acceleration on the plasma and the drag-dominated deceleration next to the plasma. As obvious from the diagram, the sign flip between acceleration and deceleration coincides with the location of velocity peak. This spatio-temporal interplay between acceleration and velocity therefore provides evidence in the above-outlined cause–effect relation between body force input $\mathrm{D}\vec{u}/\mathrm{D}t = \vec{a} \triangleq \vec{f}_{\mathrm{bf}}$ and the flow response $\vec{u}$ during acceleration.

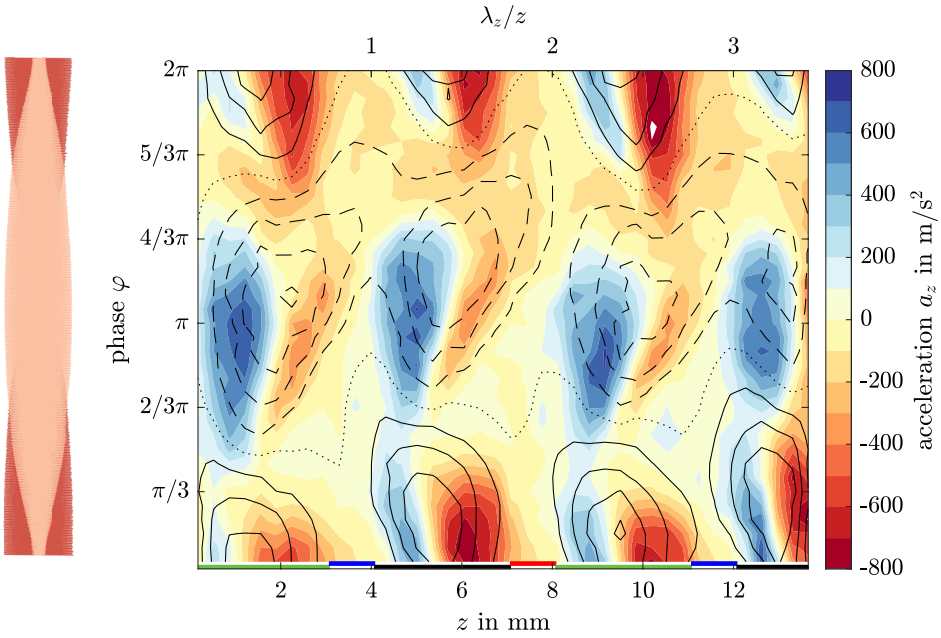

Fig. 12 Distribution of mean z acceleration profile values as surface plot with red shades representing negative and blue positive values and mean z velocity profile values as contour plot with solid lines representing negative values, dashed lines representing positive values and dotted line indicating zero over oscillation phase φ and z direction. The z velocity isolines represent 0.25 m/s steps. Electrode positions are shown for clarity, with color-coding based on electrode groups as defined in Section 1. The voltage signals over phase from Figure 5 are replotted on the left for orientation

The evaluation described above characterizes the forcing transmission behavior of the plasma-induced oscillating forcing quantitatively by relating the flow acceleration and velocity distributions, both, spatially in spanwise direction and temporally throughout the oscillation cycle. The acceleration distribution over spanwise direction and oscillation cycle peaks symmetrically at phases of maximum applied voltages, while the velocity follows a similar pattern but is shifted in time and space, quantifying the transmission inertia and convection of the flow response to the applied forcing. The spanwise expansion of the region of acceleration, indicating the momentum transfer zone, increases over the course of the oscillation halfcycles with the resulting slope in the φ-z map coinciding with the maximum of the velocity distribution, confirming the direct, causal link between body force input and resulting flow velocity.

5 Conclusions

The DPTV measurement technique is applied to measure the periodic airflow in a wall-bounded region above a PA array using a setup with only one camera. It is shown that 3D3C velocity and acceleration data can be determined by introducing a continuous tracking approach and a novel ex situ calibration procedure based on an established method by Fuchs et al. (2016), for which no prior knowledge of the flow topology or velocity data in the direct vicinity of the wall is required. For these conditions, a new procedure for the estimation of the measurement uncertainty is presented based on separate measurements in quasi-quiescent air. Since calibration and uncertainty estimation must be carried out in additional steps, the overall experimental effort increases. At the same time, the described adaptations significantly enhance the practical applicability of the measurement technique in unknown, complex flow situations. As such, great potential is shown for further studies of wall-near flow control applications, including plasma-based approaches, and (turbulent) boundary layer flows for which the region of interest is characterized by large length-to-width aspect ratios.

The measurement uncertainty is found to be strongly influenced by the choice of setup and equipment, in interaction with the processing algorithm. A compromise was made in selecting the laser, balancing available illumination with the need for high pulse frequency for time-resolved measurements. Measurement accuracy can be improved by increasing laser light intensity and camera sensitivity under consideration of the SNR, which improves PI quality and extends the range of usable PI diameters, thereby in turn enhancing the range of viable defocus sensitivities. Additionally, increasing pixel resolution is expected to further improve algorithm performance and reduce uncertainty.

The Lagrangian particle tracks are shown to allow an analysis of individually occurring events in the flow, as well as statistical effects based on extracted field data with flexible spatial and temporal resolution representing an additional benefit of DPTV as a volumetric, tracking-based measurement technique. On this basis, physical deviations of flow behavior and measurement noise can be distinguished, offering valuable insights into the coherence of the flow behavior over multiple oscillation cycles of the applied plasma-based forcing. In this context, a lateral drift in x

direction is often detected during the reversal of the forcing direction, when the particle velocity becomes very small.

The distinct electrode positions cause a discontinuous forcing along the z direction, which is observed to induce vortical motions. Moreover, the conducted measurements reveal spatially decoupled forcing impact zones for both forcing directions, which appear to be correlated in space to the oscillatory discharge extent Δz_{bf}. The forcing impact and the subsequently developing velocity fields are found to be regular between the discharge zones of the different neighboring electrode groups, indicating the applied operating voltages to be balanced across the discharge zones and the PA arrays to be manufactured with reasonable precision. However, some remaining irregularities in the distributions of velocity and acceleration uncover small effects of local forcing irregularities along the discharge zones during specific phases. Generally, the findings verify the plasma-based forcing to be capable of inducing spatially and temporally well-organized flow responses despite the highly dynamic character in the timescales of the oscillation and therefore support the application of the used PA arrays and operation concept for further parametric studies of the drag impact in turbulent flows as a next step.

The spatio-temporal relation between acceleration and velocity is evaluated quantitatively, revealing the inertia- and convection-driven forcing transmission behavior of the PA array. This analysis confirms the cause–effect relation between the plasma-induced body force input and the resulting flow response. Moreover, the inverse of the slope of maximum velocity $\partial\varphi/\partial z$ is identified to resemble the rate of change of spatial body force extent, $\partial\Delta z_{\mathrm{bf}}/\partial t$, leading to significant spanwise displacement of the resulting velocity peak during oscillation.

These insights lead to the conclusion that oscillation frequency and body force magnitude appear to span a two-dimensional parameter space, which allows to control the spatio-temporally oscillatory location of maximum spanwise velocity. Despite the observed drawback of spatially interrupted forcing with plasma actuators, this parameter space is envisioned to introduce an additional degree of freedom for the conceptualization of PA arrays and controller conception to achieve turbulent drag reduction by means of plasma-based oscillatory forcing.

Acknowledgements The authors acknowledge technical support with the Minipuls devices from SLA at TU Darmstadt.

Author contributions S. Pasch helped in conceptualization, methodology, investigation, visualization, formal analysis, data curation, writing—original draft; H.L. Lange contributed to methodology, investigation, visualization, data Curation, writing—review and editing; R. Leister helped in methodology, formal analysis, writing—review and editing; J. Kriegseis contributed to conceptualization, methodology, formal analysis, writing—review and editing, supervision, Project administration.

Funding Open Access funding enabled and organized by Projekt DEAL.

Data availability The measurement data are available upon reasonable request.

Declarations

Conflict of interest The authors declare that they have no Conflict of interest.

Open Access This article is licensed under a Creative Commons Attribution 4.0 International License, which permits use, sharing, adaptation, distribution and reproduction in any medium or format, as long as you give appropriate credit to the original author(s) and the source, provide a link to the Creative Commons licence, and indicate if changes were made. The images or other third party material in this article are included in the article's Creative Commons licence, unless indicated otherwise in a credit line to the material. If material is not included in the article's Creative Commons licence and your intended use is not permitted by statutory regulation or exceeds the permitted use, you will need to obtain permission directly from the copyright holder. To view a copy of this licence, visit http://creativecommons.org/licenses/by/4.0/.

References

Altman DG, Bland JM (2005) Standard deviations and standard errors. BMJ 331(7521):903. https://doi.org/10.1136/bmj.331.7521.903

Barnkob R, Rossi M (2020) General defocusing particle tracking: fundamentals and uncertainty assessment. Exp Fluids. https://doi.org/10.1007/s00348-020-2937-5

Benard N, Moreau E (2014) Electrical and mechanical characteristics of surface AC dielectric barrier discharge plasma actuators applied to airflow control. Exp Fluids 55(11):1846. https://doi.org/10.1007/s00348-014-1846-x

Benard N, Debien A, Moreau E (2013) Time-dependent volume force produced by a non-thermal plasma actuator from experimental velocity field. J Phys D Appl Phys 46(24):245201. https://doi.org/10.1088/0022-3727/46/24/245201

Benard N, Bonnet JP, Moreau E (2024) Drag reduction by wall-parallel standing wave with plasma actuator. In: AIAA SCITECH 2024 Forum, p 1512, https://doi.org/10.2514/6.2024-1512

Braun W, De Lillo F, Eckhardt B (2006) Geometry of particle paths in turbulent flows. J Turbul 7:N62. https://doi.org/10.1080/14685240600860923

Cierpka C, Kähler CJ (2012) Particle imaging techniques for volumetric three-component (3d3c) velocity measurements in microfluidics. J Vis 15:1–31. https://doi.org/10.1007/s12650-011-0107-9

Dreisbach M, Leister R, Probst M et al (2022) Particle detection by means of neural networks and synthetic training data refinement in defocusing particle tracking velocimetry. Meas Sci Technol 33(12):124001. https://doi.org/10.1088/1361-6501/ac8a09

Fuchs T, Hain R, Kähler C (2016) In situ calibrated defocusing PTV for wall-bounded measurement volumes. Meas Sci Technol 27(8):084005. https://doi.org/10.1088/0957-0233/27/8/084005

Fuchs T, Bross M, Kähler CJ (2023) Wall-shear-stress measurements using volumetric μPTV. Exp Fluids 64(6):115. https://doi.org/10.1007/s00348-023-03656-1

Giacosa JR, Morbelli M, Giudice G et al (2016) Spore morphology and wall ultrastructure of Lycopodiaceae from northwest Argentina.

Rev Palaeobot Palynol 225:84–94. https://doi.org/10.1016/j.revpalbo.2015.11.009
Hehner MT (2022) Dielectric-barrier discharge plasma actuators for turbulent friction-drag manipulation via spanwise oscillations. PhD thesis, Karlsruhe Institute of Technologie (KIT), 2022, https://doi.org/10.5445/IR/1000155047
Hehner MT, Gatti D, Kriegseis J (2019) Stokes-layer formation under absence of moving parts a novel oscillatory plasma actuator design for turbulent drag reduction. Phys Fluids 10(1063/1):5094388
Hehner MT, Gatti D, Mattern P, et al (2020) Virtual wall oscillations forced by a DBD plasma actuator operating under beat frequency - a concept for turbulent drag reduction. In: AIAA Aviation 2020 Forum, p 2956, https://doi.org/10.2514/6.2020-2956
Hehner MT, Gatti D, Kotsonis M et al (2022) Effects of actuation mode on plasma-induced spanwise flow oscillations. J Phys D Appl Phys 55(20):205203. https://doi.org/10.1088/1361-6463/ac526b
Hough PV (1959) Machine analysis of bubble chamber pictures. Int Conf High Energy Accel Instrum CERN 1959:554–556
Jukes T, Choi KS, Johnson G, et al (2006) Turbulent drag reduction by surface plasma through spanwise flow oscillation. In: 3rd AIAA Flow Control Conference, p 3693, https://doi.org/10.2514/6.2006-3693
Kogelschatz U (2003) Dielectric-barrier discharges: their history, discharge physics, and industrial applications. Plasma Chem Plasma Process 23(1):1–46. https://doi.org/10.1023/A:1022470901385
Kotsonis M (2015) Diagnostics for characterisation of plasma actuators. Meas Sci Technol 26(9):092001. https://doi.org/10.1088/0957-0233/26/9/092001
Kriegseis J, Schwarz C, Tropea C et al (2013) Velocity-information-based force-term estimation of dielectric-barrier discharge plasma actuators. J Phys D Appl Phys 46(5):055202. https://doi.org/10.1088/0022-3727/46/5/055202
Kriegseis J, Simon B, Grundmann S (2016) Towards in-flight applications? a review on dielectric barrier discharge-based boundary-layer control. Appl Mech Rev 68(2):020802. https://doi.org/10.1115/1.4033570
Leister R, Fuchs T, Mattern P et al (2021) Flow-structure identification in a radially grooved open wet clutch by means of defocusing particle tracking velocimetry. Exp Fluids 62(2):1–14. https://doi.org/10.1007/s00348-020-03116-0
Leister R, Fuchs T, Kriegseis J (2023) Defocusing PTV applied to an open wet clutch: from macro to micro. Exp Fluids 64(5):94. https://doi.org/10.1007/s00348-023-03623-w
Leister R, Pasch S, Kriegseis J (2023b) Defocusing PTV in a turbulent channel flow near-wall characteristics. In: 15th International Symposium in Particle Image Velocimetry
Marusic I, Chandran D, Rouhi A et al (2021) An energy-efficient pathway to turbulent drag reduction. Nat Commun 12(1):5805. https://doi.org/10.1038/s41467-021-26128-8
Olsen M, Adrian R (2000) Out-of-focus effects on particle image visibility and correlation in microscopic particle image velocimetry. Exp Fluids 29(Suppl 1):166–174. https://doi.org/10.1007/s003480070018
Pasch S, Fridlender T, Hehner MT, et al (2023) Combined and simultaneous electro-optical diagnostics for oscillatory plasma discharges. In: AIAA AVIATION 2023 Forum, p 4027, https://doi.org/10.2514/6.2023-4027
Pasch S, Leister R, Gatti D et al (2024) Measurements in a turbulent channel flow by means of an ldv profile sensor. Flow Turbul Combust 113(1):195–213. https://doi.org/10.1007/s10494-023-00469-4
Quadrio M (2011) Drag reduction in turbulent boundary layers by in-plane wall motion. Philos Trans R Soc Math Phys Eng Sci 369(1940):1428–1442. https://doi.org/10.1098/rsta.2010.0366
Raffel M, Willert CE, Scarano F et al (2018) Particle image velocimetry: a practical guide. Springer. https://doi.org/10.1007/978-3-319-68852-7
Serpieri J, Hehner MT, Pasch S et al (2023) Introducing a multi-modal plasma actuator for turbulent flow actuation. AIAA J 61(8):3707–3712. https://doi.org/10.2514/1.J062812
Wilkinson SP (2003) Investigation of an oscillating surface plasma for turbulent drag reduction. 41st Aerospace Sciences Meeting & Exhibit 2003-1023. https://doi.org/10.2514/6.2003-1023
Willert C, Gharib M (1992) Three-dimensional particle imaging with a single camera. Exp Fluids 12(6):353–358. https://doi.org/10.1007/BF00193880

Publisher's Note Springer Nature remains neutral with regard to jurisdictional claims in published maps and institutional affiliations.